Journal of Materials Chemistry A

Complex Defect Chemistry of Hydrothermally-synthesized Nb-substituted β′-$LiVOPO_4$

Journal:	*Journal of Materials Chemistry A*
Manuscript ID	TA-ART-02-2023-001152.R1
Article Type:	Paper
Date Submitted by the Author:	09-Apr-2023
Complete List of Authors:	Lee, Krystal; Binghamton University Harpur College of Arts and Sciences, Chemistry Zhou, Hui; State University of New York, Binghamton Zuba, Mateusz; Binghamton University, Physics, Applied Physics and Astronomy Kaplan, Carol; Binghamton University, Chemistry Zong, Yanxu; Binghamton University, Materials Science and Engineering Qiao, Linna; Binghamton University Zhou, Guangwen; Binghamton University, Mechanical Engineering Chernova, Natasha; Binghamton University, Liu, Hao; Binghamton University, Department of Chemistry Whittingham, Stanley; SUNY Binghamton

ARTICLE

Complex Defect Chemistry of Hydrothermally-synthesized Nb-substituted β'-$LiVOPO_4$

Received 00th January 20xx,
Accepted 00th January 20xx

DOI: 10.1039/x0xx00000x

Krystal Lee[a,b], Hui Zhou[a], Mateusz Zuba[c], Carol Kaplan[a], Yanxu Zong[c], Linna Qiao[c], Guangwen Zhou[c], Natasha A. Chernova[a], Hao Liu[*b,c], M. Stanley Whittingham[*a]

Lithium vanadyl phosphate ($LiVOPO_4$) is a next-generation multielectron battery cathode that can intercalate up to two Li-ions per V-ion through the redox couples of V^{4+}/V^{3+} and V^{5+}/V^{4+}. However, its rate capacity is undermined by the sluggish Li-ion diffusion in the high-voltage region (4 V for V^{5+}/V^{4+} redox). Nb substitution was used to expand the crystal lattice to facilitate Li-ion diffusion. In this work, Nb substitution was achieved via hydrothermal synthesis, which resulted in a new, lower symmetry β'-$LiVOPO_4$ phase with preferential Nb occupation of one of the two V sites. This phase presents complex defect chemistries, including cation vacancies and hydrogen interstitials, characterized by a combination of X-ray and neutron diffraction, elemental and thermogravimetric analyses, X-ray absorption spectroscopy, and magnetic susceptibility measurements. The Nb-substituted samples demonstrated improved capacity retention and rate capabilities in the high-voltage region, albeit an enlarged voltage hysteresis related to a partial V^{4+}/V^{3+} redox reaction, as evidenced by ex-situ X-ray absorption spectroscopy and pair distribution function analysis. This work highlights the importance of understanding the complex defect chemistry and its consequence on electrochemistry in polyanionic intercalation compounds.

1. Introduction

Li-ion battery (LIB) technology has come a long way since its commercialization in 1991. However, there is still a need for superior battery materials that can keep up with the significant growth of the grid integration and vehicle electrification markets. In present-day batteries, the leading cathodes used for energy storage on the grid and in electric vehicles are the mixed transition metal layered oxides, $LiNi_xMn_yCo_zO_2$, x + y + z = 1 (NMC). Though increasing the nickel content in NMC has improved the overall capacity and energy density, the thermal stability of the LIB becomes compromised as the material is more susceptible to oxygen release at higher states of charge. This has led researchers to revisit the more cost-effective and safer alternative, lithium iron phosphate, $LiFePO_4$ (LFP); however, the energy density is almost half that of NMC. Consequently, the main drawback of today's batteries is the cathode, which only allows for up to one electron transfer per transition metal center. Multielectron cathodes have the potential to double or even triple the energy density and capacity of current commercially-available batteries and, thus, have gained widespread attention as a contender for next-generation LIBs.[1–3]

Lithium vanadyl phosphates ($LiVOPO_4$) are a rich class of multielectron cathodes that can intercalate up to 2 Li-ions per V-ion through the redox couples of V^{4+}/V^{3+} (2.5 V vs. Li^+/Li^0) and V^{5+}/V^{4+} (4 V vs. Li^+/Li^0), translating to a specific capacity of 305 mAh/g and an energy density of over 900 Wh/kg.[2–5] The three known polymorphs of $LiVOPO_4$ are α_I (tetragonal), β (orthorhombic), and ε (triclinic), all of which can be obtained by various synthesis routes, including the solvothermal, microwave, solid-state, and sol-gel methods.[6–23] Highly crystalline ε-$VOPO_4$ nanoparticles, prepared by the solvothermal method and a subsequent annealing step, demonstrated reversible 2 Li^+ cycling per formula unit (f.u.) of $LiVOPO_4$ for up to 50 cycles when cycled at C/50 (C = 2 Li) but lost substantial capacity at higher rates in the high-voltage region.[24] However, the more favorable approach may be to employ the lithiated analog, $LiVOPO_4$, which can be synthesized easily via a one-pot, low-temperature procedure, in full-cell configurations for practical applications. The solid-state method and most multi-step syntheses involving a post-annealing step require elevated temperatures and extensive reaction times, which increases the overall cost of material production. In contrast, the solvothermal and microwave-assisted syntheses use lower temperatures (>300 °C), reducing production cost and promoting reaction homogeneity with better control over particle size and morphology. However, some limitations of conventional solvothermal synthesis include long reaction time, low product yield, and inter-batch variations, making it generally difficult to scale up for industrial production.[25] Despite

[a] NorthEast Center for Chemical Energy Storage (NECCES), Binghamton University, Binghamton, NY 13902-6000, USA
[b] Chemistry Department, Binghamton University, Binghamton, NY 13902-6000, USA
[c] Materials Science and Engineering, Binghamton University, Binghamton, NY 13902-6000, USA

† Electronic Supplementary Information (ESI) available: See DOI: 10.1039/x0xx00000x

these challenges, hydrothermal synthesis has shown to be a commercially viable method for manufacturing zeolites.[26]

The electrochemical performances of ε-$LiVOPO_4$ synthesized by these low-temperature methods have been previously reported: microwave-assisted solvothermally-synthesized (MWST) ε-$LiVOPO_4$ reached near theoretical capacity when cycled at C/10 and maintained a discharge capacity of ~250 mAh/g after 50 cycles;[22] Chung *et al.* also achieved 300 mAh/g at C/25 with hydrothermally-synthesized ε-$LiVOPO_4$. However, only about 50% of the initial capacity was retained after 20 cycles, possibly from more side reactions ensuing at slower rates.[12] As in the model ε-$VOPO_4$ material, Li-ion intercalation in all (Li)$VOPO_4$ compounds, irrespective of the synthesis route, is kinetically limited by the sluggish diffusion in the high-voltage region, corresponding to the V^{5+}/V^{4+} redox couple.

Transition metal substitution has been utilized to enhance the electrochemical performance of various cathode materials by increasing conductivity and stabilizing the crystal lattice. These efforts have been extended into (Li)$VOPO_4$ systems as a strategy to improve the reaction kinetics and electrochemical stability at high voltages (i.e., V^{5+}/V^{4+} redox).[22,27–33] In our earlier study, 3.5% Cr-substituted ε-$LiVOPO_4$ demonstrated better cycling performance than the unsubstituted material, which was attributed to increased reaction reversibility and Li-ion diffusivity in the high-voltage regime.[27] Wen *et al.* and Kaplan *et al.* both observed increased capacity and capacity retention for 5% Mo-substituted (Li)$VOPO_4$,[22,28] while Siu *et al.* noted enhanced rate performance in the high-voltage region after 1% Nb substitution of ε-$VOPO_4$.[29]

In this study, the substitution of V with Nb is implemented for its larger ionic radius and higher bond dissociation energy with O in relation to V (ΔHf_{298}(Nb-O) = 753 kJ/mol vs. ΔHf_{298}(V-O) = 618 kJ/mol).[34] It is hypothesized that Nb substitution at the V-site would enlarge the diffusion channel to facilitate faster Li-ion diffusion in the high-voltage region. Here, we systematically investigate the Nb substitutional effects on the structure, composition, and electrochemical performance of $LiVOPO_4$ prepared by a hydrothermal method.

2. Methodology

2.1. Synthesis of pristine and Nb-substituted materials. Nb-substituted $LiVOPO_4$ was synthesized by stirring vanadium pentoxide (V_2O_5, Sigma-Aldrich, >99.6%), phosphoric acid (H_3PO_4, Fisher Scientific, 85%), oxalic acid (Sigma-Aldrich), and 0, 3, 5, 7 mol.% of ammonium niobate(V) oxalate hydrate $(NH_4(C_2O_4)_2NbO{\cdot}5H_2O$, Sigma-Aldrich, >99.9%) in a 3:1 volume ratio of distilled water : ethanol. The color of the solution changed from yellow gold to light green. After 18 hours of stirring, lithium hydroxide monohydrate ($LiOH{\cdot}H_2O$, Sigma-Aldrich, >98.0%) was added, and the mixture/solution was stirred for an additional 4 hours. The solution was sealed in a 4748 Type 125 mL PTFE-lined reactor (Parr Instrument Co.) and heated in an oven at 200 °C for 48 hours. The synthesized product was collected, filtered, and washed with distilled water, ethanol, and acetone and dried at 70 °C. The final powders were dark brown. The pristine β-$LiVOPO_4$ sample (pristine HyTA) was synthesized according to published methods.[18] V_2O_5, H_3PO_4, and oxalic acid were mixed in a 3:1 volume ratio of distilled water : ethanol. The color of the solution changed from yellow gold to dark green. After 18 hours, $LiOH{\cdot}H_2O$ was added and stirred for 4 hours. The solution was heated at 160 °C for 48 hours. The synthesized product—$LiVOPO_4{\cdot}2H_2O$—was annealed at 600 °C for 3 hours under flowing oxygen to form β-$LiVOPO_4$. The final powder was green.

2.2. Materials Characterization. Scanning electron microscopy (SEM) was used to study the morphology and particle size, while energy-dispersive X-ray spectroscopy (EDX) was used for elemental detection and distribution. These samples were carbon-coated using the Ted Palla 208C High Vacuum Turbo Carbon Coater and the micrographs were collected by the Zeiss Supra-55 VP field emission SEM. Transmission electron microscopy (TEM) was collected by Thermo-Fischer Talos F200X at an accelerating voltage of 200 kV. The active particles were hand dispersed with wooden toothpicks before adhering to a copper grid with lacey carbon for electrostatic adsorption.

The metal elemental analysis was conducted using Varian Vista-MPX Axial by inductively coupled plasma optical emission spectroscopy (ICP-OES). 3-5 mg of analyte was dissolved in a mixture of oxalic acid solution and a 3:1 volume ratio of nitric acid: hydrochloric acid. Afterward, the acid mixture was diluted to 50 mL with distilled water. Carbon Hydrogen Nitrogen Sulfur (CHNS) analysis was conducted at Atlantic Microlab Inc. for hydrogen and carbon analysis.

Thermogravimetric analysis with mass spectrometry (TG-MS) was measured with a Perkin Elmer TGA 7 and a TG 209 F1 Iris coupled to a QMS 403 Aeolos Mass Spectrometer (260-TG/MS Netzsch) under flowing nitrogen at a heating rate of 10 °C/min up to 600 °C.

Fourier transform infrared spectrophotometry (FT-IR) was performed using a Shimadzu IRAffinity-1S. Made of a 100:1 mass ratio of KBr: analyte, the translucent pellets were measured in reflectance mode.

Powder X-ray diffraction (XRD) patterns were collected using a Bruker D8 Advance diffractometer with filtered Cu K radiation over the 2θ range of 10 ° to 80 °. High-resolution powder diffraction (HRXRD) data were collected at the Advanced Photon Source (APS), Argonne National Laboratory, beamline 11-BM, from 2θ range of 1 ° to 120 °, λ = 0.4579 Å. The powder sample was loaded into capillaries with a packing density of ~1.3 g/cc. Neutron powder diffraction (NPD) data were collected at the Spallation Neutron Source (SNS), Oak Ridge National Laboratory, POWGEN beamline BL-11A. The powder sample was loaded into a vanadium can with a 9.2 mm outer diameter and sealed with a copper gasket and aluminum lid. Neutron diffraction data were collected over a d-spacing range of 0.1 Å to 8 Å. Phase identification and Rietveld refinements were conducted using the PDF-2016 and TOPAS software packages, respectively.[35] References used for refinement analysis: ICDD-PDF numbers 04-012-5314 (ε-$LiVOPO_4$), 00-047-0469 (β-$LiVOPO_4$), 04-009-6369 (β-$VOPO_4$), 01-086-3810 ($LiVPO_4OH$), 04-011-4152 ($Li_4P_2O_7$).

X-ray absorption spectroscopy (XAS) data were collected at the Diamond Light Source, Harwell Science and Innovation Campus in Oxfordshire, beamline B18 at the V (5465 eV) K-edge and Nb (18986 eV) K-edges. The active material and graphite were pressed into pellets with an area of 1.2 cm^2 and sealed in Kapton tape. For the ex-situ measurements, electrodes were assembled into coin cells, charged or discharged to various potentials, and held for 6 hours. The cells were then disassembled in a glovebox, and the electrodes were sealed in Kapton tape.

The magnetic properties were measured with a superconducting quantum interference device magnetometer, Quantum Design MPMS XL SQUID. 20 - 50 mg of active material was transferred into a plastic capsule for these measurements. The temperature dependencies of the dc magnetization were measured by cooling the samples from 350 K to 2 K in a magnetic field of 1000 Oe.

X-ray total scattering measurements were carried out at beamline 11-1D-B APS, Argonne National Laboratory. The pair distribution function (PDF) was extracted using PDFgetX with a Q_{max} of 25 $Å^{-1}$.[36] All atom-atom pair identification and PDF data analysis were conducted using PDFgui and Fityk programs, respectively. For the ex-situ measurements, electrodes were assembled into coin cells, charged or discharged to various potentials, and held for 6 hours. The cells were then disassembled in a glovebox, and the electrode powders were collected and sealed in Kapton tubes.

2.3. Electrochemical Characterization. Electrodes were prepared by mixing active material, carbon additive, and PVDF in a weight ratio of 75:15:10. The active material was first high-energy ball-milled (HEBM) with graphene nanoplatelets (XG Sciences, 750 m^2/g) as the conductive additive. The powder mixture was then hand-mixed with polyvinylidene fluoride (PVDF) and 1-methyl-2-pyrrolidinone (NMP) to form a slurry. The slurry was laminated onto a carbon-coated Al foil with a mass loading of 4-6 mg/cm^2. Electrodes were assembled into coin cells in an argon-filled glove box using 2032-type coin cells (Hohsen CR2032, Japan) with a pure lithium chip (thickness 600 µm, China Energy Lithium Co.) as the anode, commercialized LP30 electrolyte (1 M $LiPF_6$ in EC:DMC (1:1), Gotion), and a Celgard 3501 separator. All electrochemical tests were conducted within a voltage window of 1.6 V - 4.5 V using a LANDdt V7 or a VMP (Bio-Logic) multichannel potentiostat. Galvanostatic charge-discharge tests were conducted using a current density of C/50 (C = 2 Li or 153 mAh/g). Cyclic voltammetry (CV) was performed at a sweeping rate of 0.25 mV/s. EIS experiments were carried out over the frequency range of 100 kHz to 1 mHz, while rate tests were conducted from C/50 to C/5, then back to C/50 for 5 cycles each. Galvanostatic intermittent titration technique (GITT) measurements were conducted within the voltage window of 1.6–4.5 V by applying current at C/20 for 1 hour and followed by 10 hours of relaxation.

3. Results and Discussion

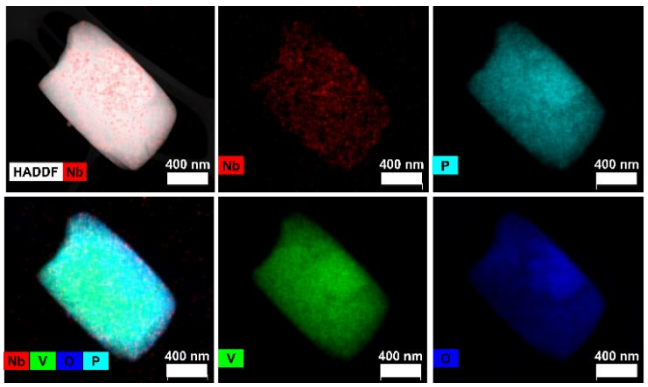

Figure 1. Elemental mapping of Nb, V, P, and O for a 5% Nb-substituted HyT $LiVOPO_4$ particle.

3.1. Morphological Characterization. SEM was used to identify the morphology and particle size of the Nb-substituted samples (x% Nb-substituted HyT, where x = 3, 5, and 7). The primary particles are 0.5 µm - 2.5 µm in size and have a smooth, rectangular prism-like morphology (Figure S1). Elemental mapping by TEM-EDS microanalysis illustrates an even distribution of Nb, V, P, and O throughout a single particle of the 5% Nb-substituted sample, suggesting successful Nb substitution (Figure 1). The unsubstituted material (i.e., pristine HyTA) is made up of irregular-shaped primary particles that agglomerate to form larger, flat secondary particles of 10 µm - 20 µm in size. It is likely that the ammonium ions introduced in the synthesis as the Nb-containing precursor significantly affect the interfacial energy, which results in the morphological differences between the pristine and substituted samples.

3.2. Composition of Nb-substituted $LiVOPO_4$. A combination of ICP-OES, CHNS, and TG-MS measurements were used to investigate the effect of substitution on the overall composition

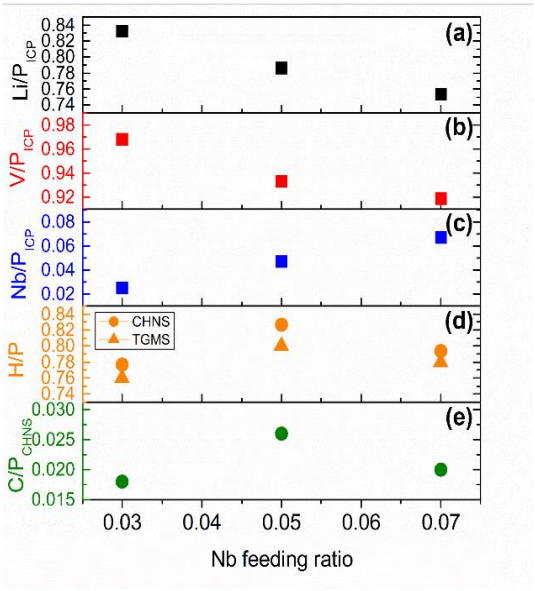

Figure 2. Elemental analysis of Nb-substituted HyT $LiVOPO_4$ samples from (a-c) ICP-OES, (d-e) CHNS, and (d) TG-MS measurements.

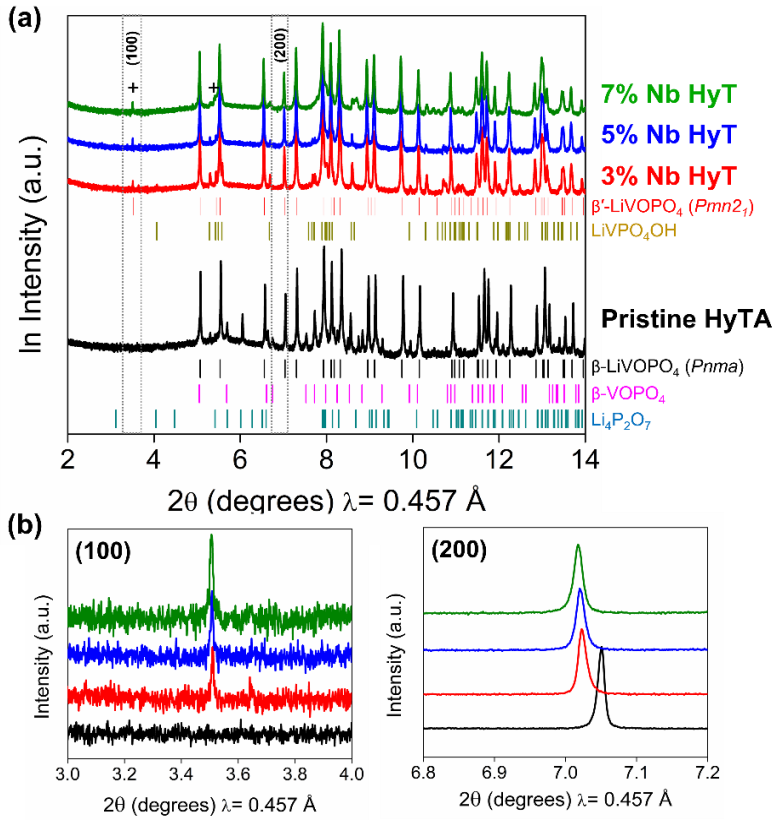

Figure 3. (a) HRXRD patterns of pristine HyTA and Nb-substituted HyT $LiVOPO_4$, and the magnified regions of the (b) (100) peaks observed for the lower symmetry β'-$LiVOPO_4$ structure with *Pmn2₁* space group.

(Figure 2, Table S1). The Nb content in the substituted samples was determined by ICP-OES (Figure 2a-c). The Nb/P ratios are 0.0248(2), 0.0468(9), and 0.0672(1) in the 3, 5, and 7% Nb-substituted samples, respectively, which agree with the feeding Nb/P ratios used in the syntheses. As the Nb/P feeding ratio increases from 3 % to 7%, the Li and V amounts decrease from 0.832(2) to 0.753(3) and from 0.968(4) to 0.919(3), respectively. CHNS measurements suggest the presence of substantial H and C with no apparent dependence on the substitution level (Figure 2d-e). However, these measurements cannot distinguish between absorbed and adsorbed species in a material. To verify the amounts of H and C in the substituted material and to determine the nature of these species, TG-MS measurements were conducted in an inert atmosphere. All weight loss is attributed to the loss of H_2O and OH^- as no appreciable emission of CO_2 is observed above the detection limit of the mass spectrometer (Figure S2). Assuming H is extracted from the structure along with stoichiometric amounts of oxygen to form H_2O, the calculated H/P molar ratios in 3, 5, and 7% Nb-substituted samples are 0.76, 0.80, and 0.78, respectively, which are in good agreement with the CHNS data (Figure 2d). The moles of H and C were normalized to P, assuming stoichiometric $LiVOPO_4$ as the sole phase after weight loss at high temperatures (supplementary note). FT-IR spectroscopy also validates the presence of H in the substituted samples, displaying a broad band at > 3000 cm^{-1} that can be assigned to the vibrational mode for O-H (Figure S3). H in the form of structural H_2O and/or protons have been proposed by previous TG-MS and CHNS analysis of various pristine and substituted $LiVOPO_4$ polymorphs synthesized by low-temperature methods.[12,22,27] The nature of H-containing species in the substituted materials will be discussed in the Sections 3.3 and 3.6.

3.3. Crystal structure of Nb-substituted LiVOPO4. Pristine β-$LiVOPO_4$ (pristine HyTA) was prepared to compare the effects of substitution, but by a two-stage procedure, since low-temperature hydrothermal synthesis yielded ε-$LiVOPO_4$ (Figure S4). The high-resolution X-ray diffraction (HRXRD) pattern of pristine HyTA is indexed to 95 wt.% β-$LiVOPO_4$ in the space group *Pnma*, 3 wt.% β-$VOPO_4$, and 2 wt.% $Li_4P_2O_7$ impurities (Figure 3). The lattice parameters are in good agreement with β-$LiVOPO_4$ synthesized by the solid-state method[8,9,14,15,18] (Figure S5), showing successful preparation of the reference material. Most Bragg peaks in the HRXRD patterns of the Nb-substituted samples can be indexed to the same β-$LiVOPO_4$ phase (*Pnma* space group) and a minority $LiVPO_4OH$ phase (< 3 wt.%). However, a weak but sharp low-angle peak (2θ = ~3.5 °, d = 7.440 Å) is observed for all substituted samples and corresponds to exactly the doubled d-spacing of the (*200*) reflection of the β-$LiVOPO_4$ phase (*Pnma*) (Figure 3b). This observation suggests that this unindexed low-angle peak can be assigned to the (*100*) reflection, which is forbidden by the glide plane in the *Pnma* space group. It is, therefore, speculated that a symmetry-lowering structural distortion of the parent *Pnma* structure is necessary to explain the (*100*) reflection.

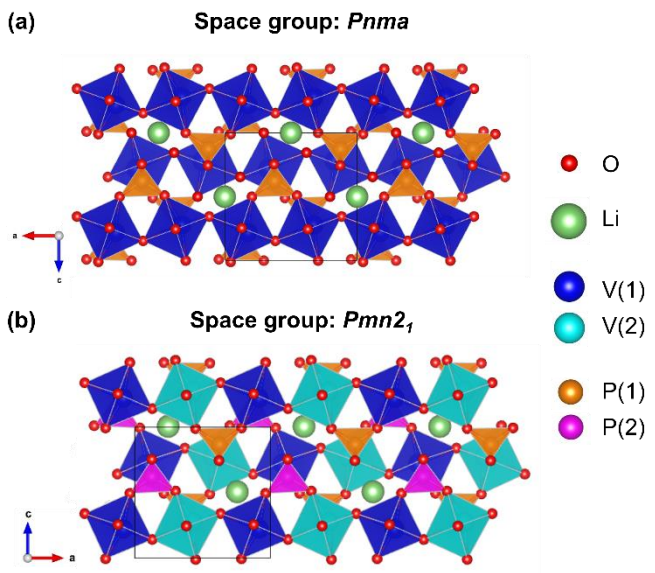

Figure 4. Structural models of (a) β-LiVOPO$_4$ (space group: *Pnma*) and (b) β′-LiVOPO$_4$ (space group: *Pmn2$_1$*). Lowering of the crystal symmetry doubles the crystallographic sites for V, P, and O. Color-coded polyhedra illustrates the two crystallographic sites for V and P in β′-LiVOPO$_4$. Black lines indicate unit cells.

ISOTROPY[37] was used to explore the structural distortion in the isotropy subgroup of *Pnma* and suggests a distorted structure with the *Pmn2$_1$* space group, denoted as β′-LiVOPO$_4$, as the best candidate to explain all observed Bragg reflections. The lack of the glide plane in β′-LiVOPO$_4$ doubles the crystallographic sites for V, P, and O found in β-LiVOPO$_4$ (*Pnma* space group) (Figure 4). While all the V-sites in β-LiVOPO$_4$ are crystallographically equivalent, two crystallographically distinct VO$_6$ octahedra in β′-LiVOPO$_4$ alternate along the vanadium chain (along the *a*-axis) in the lower symmetry phase (*Pmn2$_1$*). The PO$_4$ tetrahedra of β-LiVOPO$_4$ connect the VO$_6$ chains in either the "up" or "down" orientation and are crystallographically equivalent. In contrast, the "up"-oriented PO$_4$ tetrahedra of β′-LiVOPO$_4$ are crystallographically different from "down"-oriented tetrahedra. Since the number of distinct Li sites is preserved in the lower symmetry structure, the structural distortion must be caused by occupational and/or displacement distortion between the two V and P sites in β′-LiVOPO$_4$. Given the large formation energy of the P Schottky defect in phosphates,[38] the structural distortion is likely caused by differences between the two V sites.

The unit cell parameters of the Nb-substituted samples were determined from the Rietveld refinement against the HRXRD patterns and plotted as a function of the Nb feeding ratio (Figure S6). The lattice parameters of the substituted phases are significantly larger than the non-substituted sample, resulting in a 1.18% volume expansion after 3% Nb substitution (**Figure S5**). A similar volume of ~340 Å^3 was reported for MWST-synthesized 5% Nb-substituted LiVOPO$_4$.[22] In comparison, 10% Nb substitution in ε-VOPO$_4$ resulted in only 0.6% volume expansion.[29] As Nb substitution increases from 3% to 7%, all lattice parameters and unit cell volume increase linearly, but it is important to note that these changes are less significant. While changes in the lattice parameters are often employed to infer the degree of substitution, the presence of multiple and confounding structural defects (i.e., Li and V vacancies) besides Nb substitution does not warrant the simple application of Vegard's law.

Neutron powder diffraction (NPD) was performed for the Nb-substituted samples to complement the HRXRD data to determine the crystal structure (Figure 5). The (*100*) reflection of β′-LiVOPO$_4$ phase is not observed, likely due to the lower signal-to-noise ratio of NPD than the HRXRD. The large contrast in the neutron scattering length between V (-0.3824 fm) and Nb (7.054 fm) and the appreciable scattering length of hydrogen (H) complements the XRD data in the analysis of Nb substitution and potential H incorporation in the crystal structure. The high background in the low Q region of the neutron diffraction data is attributed to the inelastic incoherent scattering of hydrogen[39], but it cannot be deduced that H is also present in the primary phase since an impurity hydroxide phase is also present in the sample from the HRXRD result. However, Rietveld refinement of the β′-LiVOPO$_4$ structure (space group *Pmn2$_1$*) without H shows a noticeable mismatch in the high d-spacing (low Q) region (Figure S7a), which indicates substantial discrepancy between the refined structure model and the actual crystal structure. Fourier difference map analysis (Figure S8) reveals substantial negative scattering lengths around the oxygen atoms bridging the vanadium atoms, which can only be accounted for by H in the crystal structure. Adding hydrogen atoms to the positions identified in the Fourier difference map significantly improves the profile fitting in the high d-spacing (low Q) region (Figure S7b). Therefore, a substantial amount of H is incorporated in the crystal structure.

To determine the occupancy of the V and Li sites in the substituted structure, it is necessary to consider co-occupation by all possible species, which include Li, V, Nb, and vacancies. The HRXRD and NPD data alone cannot determine such complex mixed site occupation. Analysis of the refined scattering power/lengths for the V and Li sites suggests the co-occupation of Nb at the V 2a sites and vacancies and TM at the Li 4b site (Figures S9-S11, supplementary note). Therefore, for the combined refinement against the XRD and NPD data, the structure model assumes only V, Nb, and vacancy at the V 2a sites and Li, V (or Nb), and vacancy at the Li 4b site.

The structure parameters based on the joint Rietveld refinements are listed in Tables 1 and S2-S3. The results show different V occupancies at the two V 2a sites, where less V occupies the V(1) site than the V(2) site. The disparity in the V occupancy between the two V 2a sites in β′-LiVOPO$_4$ increases with higher Nb substitution levels, however, the average V occupancy is effectively the same regardless of Nb substitution. As for the substituent, Nb preferentially occupies the V(1) site, and the average Nb occupancy increases from 0.008(5) for the 3% to 0.03(1) for the 7% Nb-substituted samples. The refinement results also show the co-occupation of the Li site by heavier elements (i.e., V and/or Nb), yet it is inconclusive whether V or Nb is the primary species that occupy the Li 4b site. It is noted that the Li occupancies are 0.884(0), 0.88(1), and

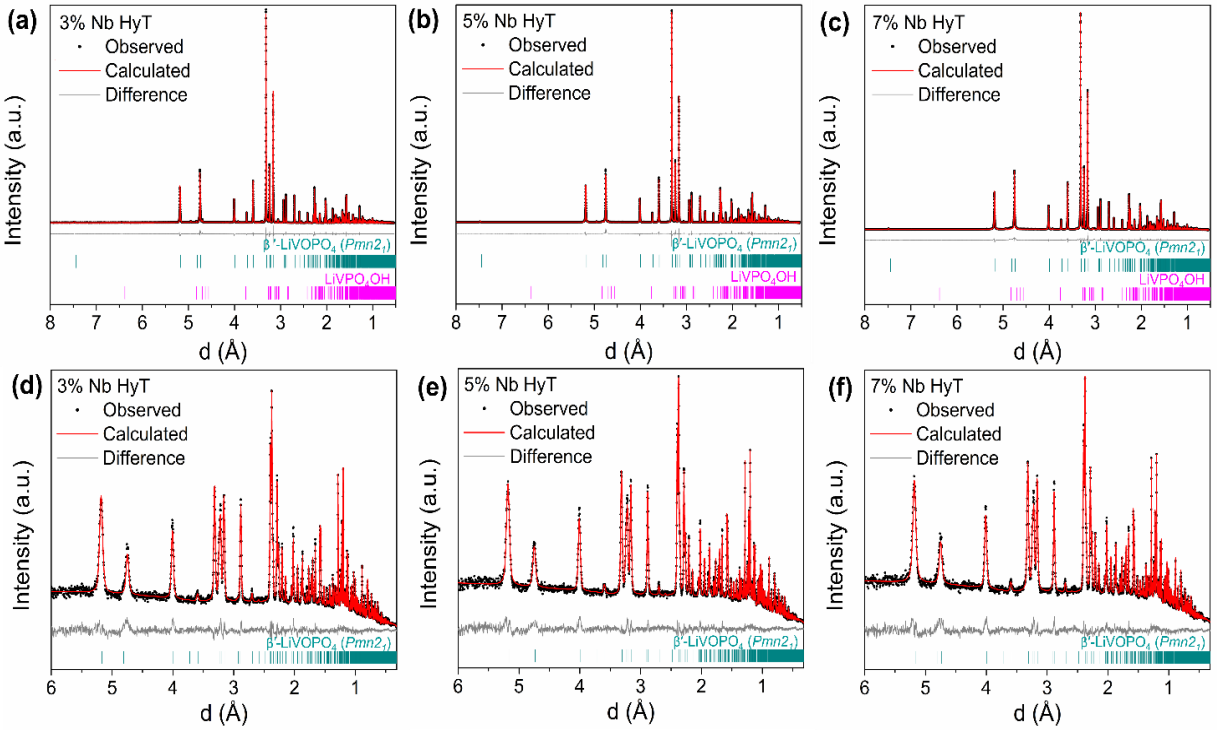

Figure 5. Joint Rietveld refinement against the (a-c) HRXRD and (d-f) NPD patterns of Nb-substituted HyT $LiVOPO_4$. Black points correspond to the observed intensities, solid red lines correspond to the calculated intensities, and solid gray lines indicate the difference between these intensities.

Table 1. Structural parameters obtained from combined Rietveld refinement against the HRXRD and NPD patterns of 5% Nb-substituted HyT $LiVOPO_4$.

5% Nb-substituted HyT						
SG = *Pmn2₁*	*a* = 7.4778(1) Å			R_{wp} = 3.91 %		
β′-$LiVOPO_4$ = 98.83 %	*b* = 6.3272(7) Å			R_{exp} = 2.51%		
$LiVPO_4OH$ = 1.17 %	*c* = 7.1948(9) Å					
	Vol = 340.413(9) Å3					
Atoms	**X**	**y**	**z**	**Occupancy**	**Wyckoff position**	**ADP (Å²)**
V(1)	0.0865(1)	0	-0.2800(2)	0.87(1)	2a	0.663(8)
Nb(1)	0.0865(1)	0	-0.2800(2)	0.03(1)	2a	0.663(8)
V(2)	0.5747(1)	0	-0.2267(2)	0.92(2)	2a	0.663(8)
Nb(2)	0.5747(1)	0	-0.2267(2)	0.02(1)	2a	0.663(8)
Li(1)	0.754(1)	0.740(1)	0.504(1)	0.89(1)	4b	1.29(6)
V(3)	0.754(1)	0.740(1)	0.504(1)	0.029(1)	4b	0.663(8)
P(1)	0.3771(3)	0	-0.6334(3)	1	2a	0.546(7)
P(2)	0.8757(2)	0	-0.8797(3)	1	2a	0.546(7)
O(1)	0.0369(3)	0	-0.0077(4)	1	2a	0.751(6)
O(2)	0.5523(3)	0	-0.5131(4)	1	2a	0.751(6)
O(3)	0.1248(3)	0.6964(5)	-0.2469(4)	1	4b	0.751(6)
O(4)	0.6205(3)	0.3057(4)	-0.2576(4)	1	4b	0.751(6)
O(5)*	0.8716(4)	0	-0.3603(5)	1	2a	0.751(6)
O(6)*	0.3686(4)	0	-0.1628(4)	1	2a	0.751(6)
O(7)	0.2150(3)	0	-0.5077(4)	1	2a	0.751(6)
O(8)	0.7004(3)	0	0.0094(4)	1	2a	0.751(6)
H(1)	0.021(2)	0.445(3)	0.146(3)	0.192(7)	4b	1
H(2)	0.661(3)	0.638(4)	0.447(3)	0.149(8)	4b	1

*The oxygens in the closest proximity to H

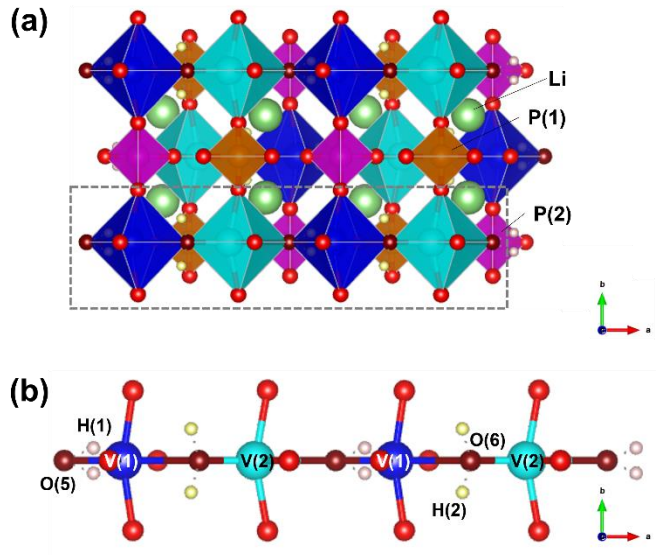

Figure 6. (a) Structure of 5% Nb-substituted HyT β′-$LiVOPO_4$ based on combined Rietveld refinement against the HRXRD and NPD patterns and (b) the magnified region of the vanadium chain. $V(1)O_6$ and $V(2)O_6$ octahedra in blue and teal, respectively; $P(1)O_4$ and $P(2)O_4$ tetrahedra in orange and magenta, respectively; H(1) and H(2) in pale pink and yellow, respectively; Li atoms in green; O(5) and O(6) bonded to H in dark red; all other O atoms in red.

Nb, occupies the Li 4b site. Still, the refined occupancies are considerably different from the values determined by elemental analysis (Table S4), which could be caused by the inherent limitation of the structure model that can only determine the mixed site occupation by up to two different species. Nonetheless, the diffraction data shows the successful substitution of Nb at the V site.

Two crystallographically distinct positions for H are identified near the bridging oxygen atoms, O(5) and O(6) at (0.01, 0.40, 0.10) and (0.68, 0.60, 0.46), respectively, with O-H bonds lengths ranging between 0.9 Å - 1.3 Å (Figure 6). These findings align with the H positions detected along the TMO_6 chain in tavorite V/Fe phosphate compounds (e.g., $LiVPO_4OH$,[40] $FePO_4{\cdot}H_2O$[41]) by neutron diffraction and those evaluated in the ε-$VOPO_4$ structure by first-principles calculations.[42] H occupancy in both sites increases with higher substitution levels: occupancy increases from 0.113(4) to 0.217(7) in the H(1) site and from 0.106(4) to 0.16(1) in the H(2) site when the Nb feeding ration increases from 3% to 7%. The overall H content in the crystalline β′-$LiVOPO_4$ phase is less than the values determined by CHNS and TG-MS, which suggests that H in the substituted phase may not be the sole hydrogen source. It is worth mentioning that a discrepancy was also noted between the stoichiometric amount of H in H_2VOPO_4 and the amount deduced from sample weight loss by TGA analysis in previous reports, where Lim *et al.* attributed this discrepancy to adsorbed organic impurities from the synthesis procedure,[43] while Vaughey *et al.* speculated the difference to be from disordered H_2O molecules in the material.[44] However, neither study provided structural evidence for the origin of the hydrogen in their samples. Our diffraction results do not support the presence of structural water in the Nb-substituted samples since both HRXRD and NPD data are well-fitted with the refined structure model that does not include structural water. The cavities in the structure of the Nb-substituted samples are likely too small to accommodate H_2O molecules. It is noted that previous reports of structural water have been limited to the layered (Li, K)$VOPO_4$ polymorphs.[45,46]

The TM-O and P-O bond lengths from the combined refinement and X-ray PDF results were used to analyze the changes in the local structure with increasing Nb substitution (Table S5). In β-$LiVOPO_4$, P-O bonds of the phosphate group are similar in length (1.54 Å on average), while the VO_6 units are made up of one short (1.63 Å) and one long (2.34 Å) V-O bonds, and four equatorial bonds that are closer in length with an average of 1.97 Å.[8] Since Nb is substituted at the V site, the bonds coordinated to the V 2a sites will be denoted as TM-O. The average P-O and TM-O bond lengths of the Nb-substituted samples, obtained from the combined refinement results, are consistent with these reports[8] and remain essentially the same irrespective of Nb concentration, suggesting the oxidation state of V in the substituted samples is primarily +4. All substituted samples display average bond lengths of ~1.97, 1.66, and 2.34 Å for the equatorial ($TM\text{-}O_{eq}$) and the short and long axial TM-O bonds, respectively (Figure 7, indicated in black). However, all TM(1)-O bonds are generally smaller than the TM(2)-O bonds of the substituted samples (Figure 7b-d). The dimensions of the $Nb^{5+}O_6$ octahedra are slightly larger than the $V^{4+}O_6$ octahedra; the preferred coordination sphere of NbO_6 comprises four medium-length bonds with an average of 1.98 Å and slightly longer short (1.75 Å) and long (2.37 Å) Nb-O bonds.[47] Hence, Nb substitution and vacancies at the V site are expected to have opposing effects on the octahedron dimension, causing the TM-O lengths to elongate and contract, respectively. Therefore, the overall reduction in the TM(1)-O bond lengths suggests the contributions from vacancies likely outweigh those from Nb occupation, which is supported by higher concentrations of vacancies, compared to Nb, at the V(1) site in the substituted samples (Tables 1 and S2-S3). With increasing Nb feeding ratio, the P(1)-O bond elongates (from 1.538 Å to 1.552 Å), while P(2)-O bond contracts (from 1.538 Å to 1.528 Å). Additionally, the short TM(1)-O(5) bond elongates (from 1.579 Å to 1.642 Å) as the TM(2)-O(6) bond contracts (from 1.735 Å to 1.669 Å) from 3 % to 7% Nb substitution, while the long TM(1)-O(6) bond contracts (from 2.297 Å to 2.280 Å) as the TM(2)-O(5) bond slightly elongates (from 2.411 Å to 2.415 Å). These results further illustrate the disparity between the two crystallographically distinct V and P sites, by which a significant proportion of structural distortion can be attributed to disparate V site vacancies, which lowers the symmetry of the parent *Pnma* structure.

X-ray PDF analysis of the Nb-substituted samples verifies the results from combined refinement, showing the average P-O and $TM\text{-}O_{eq}$ bond lengths remain largely the same with increasing substitution (Figures S12-S13). The FWHM of Peak 1 (1.57 Å, assigned to P-O correlation) increases as Peak 2 (1.99 Å,

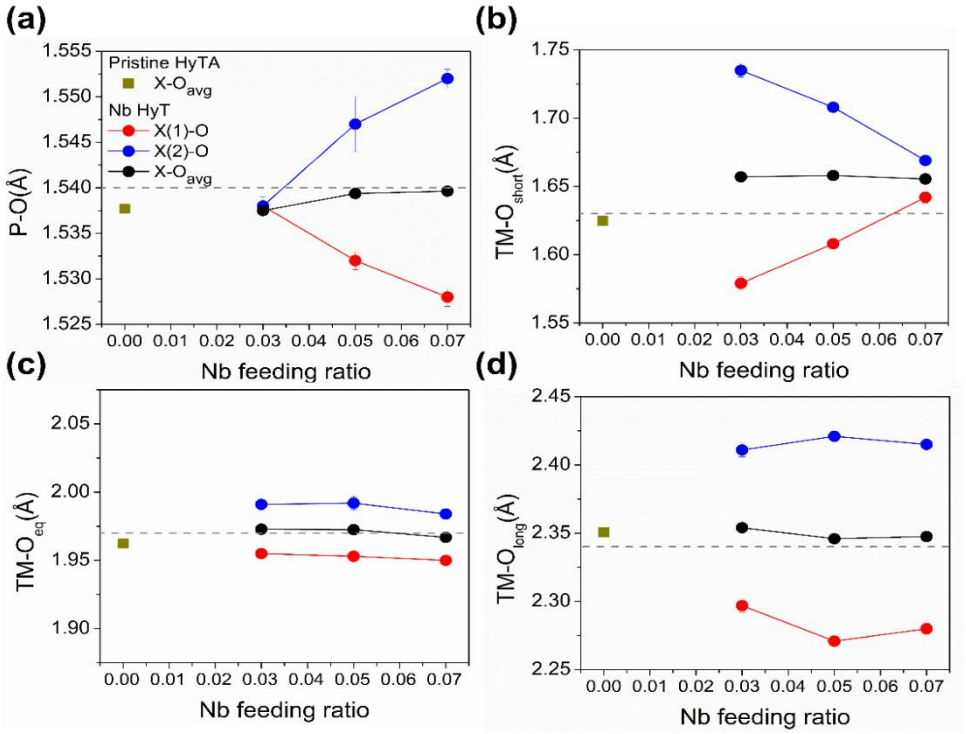

Figure 7. Bond lengths of (a) P-O and the (b) short, (c) equatorial, and (d) long TM-O obtained from combined Rietveld refinement against the HRXRD and NPD patterns of pristine HyTA and Nb-substituted HyT LiVOPO$_4$. Dashed lines correspond to the bond lengths of β-LiVOPO$_4$ from the literature.[8]

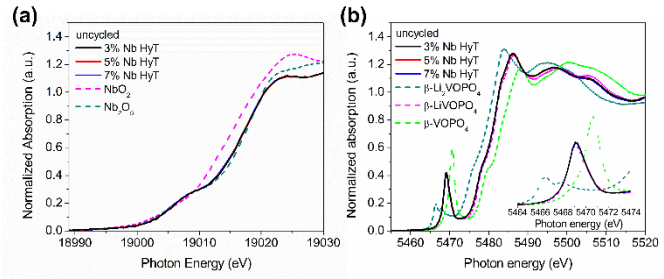

Figure 8. XAS spectra at the (a) Nb and (b) V K-edges (inset shows the enlarged pre-edge region) of Nb-substituted HyT LiVOPO$_4$.

assigned to TM-O correlation) decreases, representing the increased spread of the P-O bond lengths and decreased spread of the TM-O bond lengths with increasing Nb substitution. These observations are consistent with the joint refinement results (Table S5), where the range of distinct P-O bond lengths increases (Δ = from 0.02 Å to 0.07 Å) and those of TM-O$_{eq}$ bond lengths decreases (Δ = from 0.17 Å to 0.13 Å) with increasing Nb substitution.

3.4. X-ray absorption spectroscopy study. XAS was used to determine the oxidation states of the TMs in the substituted material. The V and Nb K-edge XANES spectra of the substituted samples (Figure 8) were compared to reference compounds with well-defined Nb^{4+}, Nb^{5+}, V^{3+}, V^{4+}, and V^{5+} oxidation states. At the Nb K-edge, the pre-edge and absorption edge of all substituted samples overlap more closely with that of the Nb_2O_5 standard, indicative of a Nb^{5+} oxidation state in the bulk (Figure 8a). As for V, the pre-edge peak position at the V K-edge is at the same energy for the β-LiVOPO$_4$ standard (5469 eV) along with similar peak intensities, suggesting the V oxidation state is predominantly +4, which is consistent with the combined refinement and X-ray PDF results.

3.5. Magnetic susceptibility study. To complement the XAS study of the oxidation state of the transition metal ions, magnetic susceptibility measurements were conducted to determine the amount of V^{3+} and V^{4+}, which are the only paramagnetic ions in the Nb-substituted samples. The substituted samples exhibit Curie–Weiss behavior at high temperatures and ferrimagnetism at low temperatures, consistent with that reported for hydrothermally-synthesized ε-LiVOPO$_4$ (Figure 9).[12,27] The high-temperature regime of the susceptibility curve was fit with the Curie-Weiss Law, and the resulting parameters are provided in Table S6. The negative Curie-Weiss temperatures suggest predominantly antiferromagnetic interactions, similar to what is observed in high-temperature synthesized, stoichiometric ε-LiVOPO$_4$.[12,48] However, an increase in magnetic susceptibility below 15 K is indicative of a small ferrimagnetic moment (Figure 9**a**). A change in magnetic behavior from ferrimagnetic to antiferromagnetic was observed after the removal of structural defects from hydrothermally-synthesized ε-LiVOPO$_4$ through high-temperature heating.[12] Therefore, the ferrimagnetic behavior of the Nb-substituted samples is likely due to the disorder introduced by the defects described in Section 3.3. It should be noted that spin-glass-like behavior is also possible due to structural disorder. However, spin glasses typically show

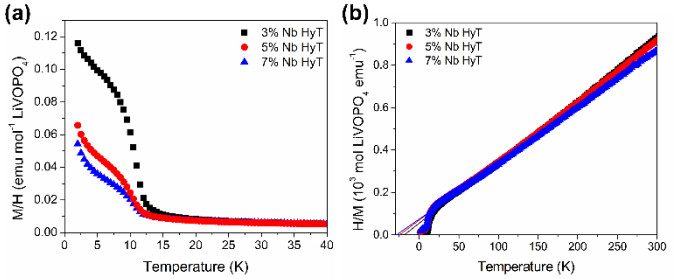

Figure 9. (a) Temperature dependencies of the magnetic susceptibilities and the (b) inverse for Nb-substituted HyT $LiVOPO_4$ fitted to the Curie-Weiss law

a broad susceptibility maximum,[49] which is not observed for the Nb-substituted samples.

Diamagnetic Nb^{5+} and V^{5+} ions (d^0, S = 0) are expected to make negligible contributions to the magnetic susceptibility, and therefore, only the spin contributions of V^{4+} (d^1, S = 1/2) and V^{3+} (d^2, S = 1) were considered. To obtain the effective magnetic moment, two compositional models – one based on the elemental analysis (ICP-OES) and the other based on the refined occupancies from the diffraction analysis – were adopted to normalize the experimental Curie constants given the disparate compositions derived from these two methods (supplementary note). For both compositional models, the effective magnetic moments (Figure S14, Table S7) decrease with higher Nb substitution, ascribing to the increase in diamagnetic Nb^{5+} concentration. The effective magnetic moments are 1.73, 1.69, and 1.68 μB for the 3, 5, and 7% Nb-substituted samples, respectively, when the ICP-OES-determined TM amounts are used to normalize the Curie constants. In comparison, the effective magnetic moments are 1.77, 1.71, and 1.70 μB for the 3, 5, and 7% Nb-substituted samples, respectively, when the Curie constants are normalized to the TM amounts determined by Rietveld refinement. Though analysis with both compositional models suggest an increase in Nb^{5+} concentration, the effective magnetic moments normalized to the ICP-OES-determined TM content agree better with the effective moment based on the target stoichiometry from the synthesis (i.e., $LiNb_{0.03}V_{0.97}PO_4$, $LiNb_{0.05}V_{0.95}PO_4$, and $LiNb_{0.07}V_{0.93}PO_4$ for the 3, 5, and 7% Nb samples). The effective magnetic moments for the target stoichiometry decrease from 1.71 μB for the 3% to 1.67 μB for the 7% Nb-substituted samples. The composition derived from diffraction analysis may not be accurate because it does not account for the impurity or possible amorphous phases also present in the sample. Therefore, ratios of V^{3+}/P and V^{4+}/P were calculated from the experimental effective magnetic moments based on the ICP-OES stoichiometry. The V^{4+} concentration decreases from 0.950(3) for the 3% to 0.912(0) for the 7% Nb-substituted sample. No substantial amounts of V^{3+} (less than 0.018(0)) are observed for any of the samples.

3.6. Charge compensation mechanism of Nb-substituted $LiVOPO_4$. The composition of the Nb-substituted samples was evaluated using the collective results from ICP-OES, CHNS, XAS, and SQUID measurements. The total cationic charges were calculated using the oxidation states of Li^+, Nb^{5+}, and V^{4+}. Anionic defects were not considered in this study, and H^+ is introduced to achieve charge neutrality. The compositions based on these assumptions are summarized in Table S8. The amount of H necessary to reach a charge-neutral system generally increases with higher substitution levels, from 0.170 per f.u. for the 3% to 0.232 per f.u. for the 7% Nb-substituted samples. This result is in good agreement with the refined H compositions in these samples based on the diffraction data (0.219(0), 0.341(0), and 0.37(7) per f.u. in the 3, 5, and 7% Nb-substituted samples, respectively). However, this still leaves a substantial amount of H (0.55-0.61 H/P determined from CHNS analysis) unaccounted for by the impurity hydroxide phase (less than 3 wt. %) detected in these samples. Such excess H has also been reported for MWST-synthesized pristine and substituted β- and ε-$LiVOPO_4$, which was ascribed to structural water that does not participate in charge compensation.[22] If the excess H were attributed to structural water in the crystal structure, there would be 0.28-0.31 per f.u. in the substituted samples. However, neither HRXRD nor NPD support the presence of H_2O molecules as discussed in Section 3.3. Therefore, we rule out the presence of structural water in the Nb-substituted β'-$LiVOPO_4$ phase, and further investigation is needed to identify the origin of the remaining H in the substituted samples.

3.7. Electrochemical Performance. To compare their electrochemical performance, all samples were ball-milled with conductive carbon to ensure similar particle size, a factor that can impact the rate of Li-ion diffusion. SEM images of the post-ball-milled samples (Figure S15) show that the particle sizes are reduced from micron- to nano-scale. A series of tests were conducted to investigate the electrochemical behavior of the Nb-substituted samples. The coin cells were first discharged to 1.6 V and then cycled between 1.6 V - 4.5 V at C/50. The behavior of 2 Li^+ cycling is typically partitioned into the low-voltage (1.6 - 3.0 V) and high-voltage (3.0 - 4.5 V) regions.[24,50] The galvanostatic charge-discharge test of pristine HyTA displays a voltage profile and performance similar to solid-state β-$LiVOPO_4$ (Figure 10). This sample shows a single plateau at ~4 V in the high-voltage region, representing a two-phase reaction associated with the V^{5+}/V^{4+} redox, along with features below 3 V in the low-voltage region, corresponding to multiple two-phase reactions attributed to the $V^{4+}/^{3+}$ redox reaction.[50] The pristine HyTA sample reaches initial charge and discharge capacities of 292.6 mAh/g and 280.1 mAh/g, respectively, which translates to a Coulombic efficiency (CE) of 95.5 %. In comparison, β-$LiVOPO_4$ synthesized by Hidalgo *et al.* demonstrated a slightly lower initial discharge capacity of ~275 mAh/g with a corresponding CE of ~91.3% at C/40.[18] Cycled at xC/10, β-$LiVOPO_4$ prepared via the sol-gel method by Zhou *et al.* reached capacities of ~250 mAh/g, the relatively fast rate likely responsible for the reduced capacities.[14] The galvanostatic tests of the Nb-substituted samples display a different set of electrochemical voltage profiles. The low-voltage profile becomes a slope, which indicates the disruption of the Li-vacancy orderings that underpin the series of voltage plateaus observed for the non-substituted β-$LiVOPO_4$. An extra voltage plateau emerges at ~3.5 V during the charging process. Both

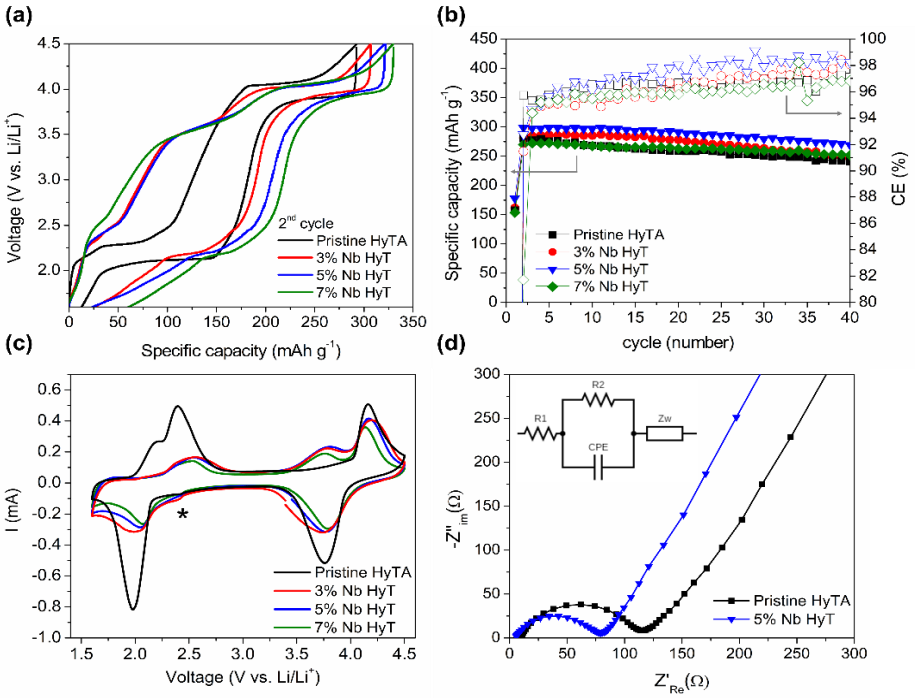

Figure 10. (a) Voltage profile, (b) cycling performance and Coulombic efficiency for 40 cycles at C/50, and (c) cyclic voltammogram of pristine HyTA and Nb-substituted HyT $LiVOPO_4$. (d) Impedance spectra and equivalent circuit model of pristine HyTA and 5% Nb-substituted HyT $LiVOPO_4$. In the high-frequency region, the bulk resistance (R1) is associated with the resistance of the cell components and the electrolyte. CPE, the constant phase element, refers to the capacitance associated with the dielectric constant of a specific active material, while R2 describes the resistance across the electrode-electrolyte interface and the charge transfer resistance. The Warburg impedance (Z_w) in the low-frequency region is related to Li^+ diffusion into the bulk, represented by a slope at 45 °.

changes are associated with substantial voltage hysteresis, readily observed in the cyclic voltammograms (Figure 10c). The shoulder at 2.2 V of the cathodic peak observed in pristine HyTA disappears in Nb-substituted samples, while an additional cathodic peak emerges at 3.5 V. The nature of this 3.5 V process is discussed in Section 3.8. The qualitative difference in the voltage profile after substitution suggests a unique reaction mechanism for the Nb-substituted material, which may be attributed to its complex defect chemistry as revealed by the ICP-OES and HRXRD/NPD results. However, the high-voltage V^{5+}/V^{4+} process is not affected in the Nb-substituted sample except for the slightly decreased capacity. Regarding discharge capacity, the Nb-substituted samples demonstrate slightly higher initial capacities than the pristine material, with the 5% Nb-substituted sample reaching the highest discharge capacity of 298.4 mAh/g. A correlation between Nb content and cycling stability is also observed, where the retention rate after 40 cycles improves with substitution, increasing from 87.2% for the 3% to 93.4% for 7% Nb-substituted samples. EIS measurement was performed for the pristine and 5% Nb-substituted samples to quantify the bulk resistivity and interfacial charge transfer (Figure 10d, the inset shows the equivalent circuit model). The impedance spectra show that while the R_1 values (ascribed to the resistance of the cell components and the electrolyte) of the samples are comparable (8.91 Ω and 4.80 Ω for pristine and 5% Nb-substituted samples, respectively), the R_2 value (ascribed to the resistance across the electrode-electrolyte interface and the charge transfer resistance) of the 5% substituted material (74.09 Ω) is considerably lower than the reference sample (105.30 Ω), indicating improved Li^+ migration in the substituted sample.

Rate performance tests were conducted within separate voltage windows of 3.0 V - 4.5 V and 1.6 V - 3.0 V to evaluate the high- and low-voltage intercalation kinetics, respectively, of the substituted samples (Figure 11). In the high-voltage (3.0 - 4.5 V) window, all substituted samples, including the 7% Nb-substituted sample that demonstrated the lowest initial capacity, maintain or reach higher capacities than the reference sample when cycled at a faster rate than C/50. At C/5, the reference sample retains 75% of the total capacity observed during C/50 cycling, and the substituted samples exhibit a slightly higher retention rate of 80%, suggesting improvement in the kinetically limited-high voltage reactions by Nb substitution. GITT measurements validate this enhancement in the high-voltage region. The Nb-substituted HyT sample experiences a smaller overpotential than the pristine HyTA sample, which shows a more considerable voltage change when discharged below 3.7 V (Figure S16). In contrast, the capacities in the low-voltage (1.6 - 3.0 V) window rate performance tests decrease with increasing substitution levels, irrespective of the current rate. It is noted for the Nb-substituted electrodes that the sum of the capacities measured for the separate voltage windows (e.g., 210 mAh/g for 5% Nb-substituted sample) is substantially less than the capacity measured for the full-voltage window (e.g., 300 mAh/g for 5% Nb-substituted sample). Shown in the insets in Figure 11, ~1.95 Li^+

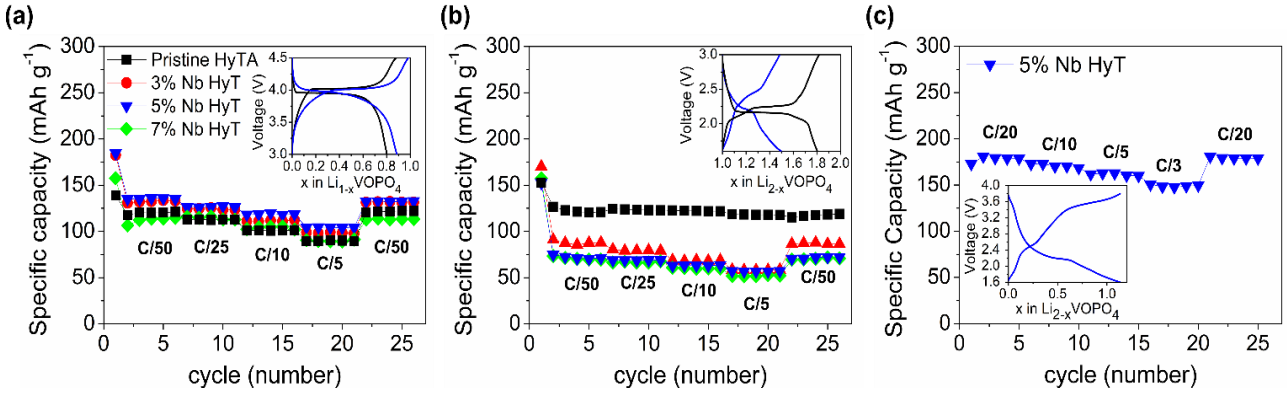

Figure 11. Rate performance of pristine HyTA and Nb-substituted HyT $LiVOPO_4$ in the (a) high-voltage (3.0 - 4.5 V), (b) low-voltage (1.6 - 3.0 V), and (c) adjusted low-voltage (1.6 - 3.8 V) windows. The insets show the galvanostatic curves.

(de)intercalation is possible when cycled within the full-voltage window of 1.6 V - 4.5 V, but only 0.9 and 0.5 Li^+ (total of 1.4 Li^+) (de)intercalation is observed for the substituted material when cycled within the respective high- and low-voltage regions. A comparison of the voltage profiles for the separate (1.6 - 3.0 V and 3.0 - 4.5 V) and the full-voltage windows (1.6 - 4.5 V) reveals the absence of the 3.5 V plateau (with a capacity of 80 mAh/g) in the high-voltage window (3.0 - 4.5 V) cycling, which explains the discrepancy in the capacity observed when cycling in separate voltage windows. Upon widening the low-voltage window to 1.6 V - 3.8 V, the 3.5 V feature re-emerges, increasing the low-voltage capacity to 173 mAh/g that better matches the full-voltage cycling results and is closer to the expected value of 1 Li^+ per f.u. This suggests that the 3.5 V feature is associated with the low-voltage V^{4+}/V^{3+} redox couple.

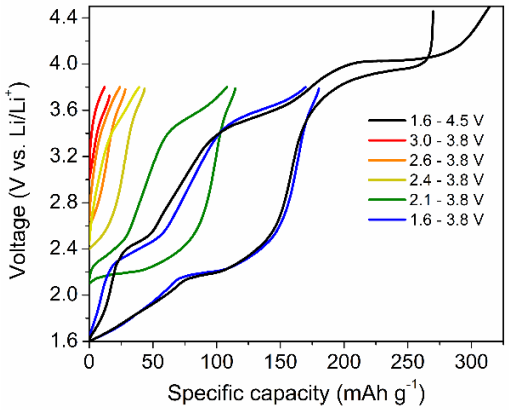

Figure 12. Galvanostatic charge and discharge curves of 7% Nb-substituted HyT $LiVOPO_4$ from varying lower cut-off potentials to 3.8 V.

3.8. Origin of 3.5 V redox reaction. Additional galvanostatic tests were conducted within various electrochemical windows to gain a better understanding of the electrochemical origin of the 3.5 V redox reaction during the charging process. Figure 12 shows the galvanostatic charge-discharge curves of the 7% Nb-substituted sample cycled from a constant upper voltage cut-off of 3.8 V to decreasing lower voltage cut-offs of 3.0, 2.6, 2.4, 2.1, and 1.6 V. A comparison of the voltage profiles indicates the plateau at 3.5 V only begins to appear when the lower cut-off voltage is set below 2.6 V. This feature becomes more pronounced with deeper discharge (i.e., decreasing lower cut-off voltage), leading to increased capacity. The CV data (Figure 10c) suggests the reduction reaction in the low-voltage region at ~2.6 V (indicated by *) is responsible for the subsequent oxidation at 3.5 V, which is consistent with the variable cut-off voltage cycling result (Figure 12). Hence, the oxidation peak at 3.5 V and the reduction peak at 2.6 V correspond to the same redox couple, likely involving the redox of +4 and lower valent V-ions or the redox of Nb ions.

The XANES spectra (Figure 13 and S17) were collected at the V and Nb K-edges at various states of charge and discharge to investigate changes in the oxidation state and the charge compensation mechanism upon cycling as well as to study the redox activity in the Nb-substituted samples. At the Nb K-edge, the pre-edge tail (19016 eV) of 7% Nb-substituted noticeably shifts to lower energies once the sample is fully discharged to 1.6 V, ascribed to Nb^{5+} reduction (Figure 13c). Upon charging to 4.5 V, this pre-edge feature is restored to that of the uncycled sample, which shows that reduction of Nb^{5+} occurs at < 3 V (vs. Li^+/Li^0). This observation is consistent with the calculated Nb^{5+}/Nb^{4+} reduction potentials (~2.5 V vs. Li^+/Li^0)[5] and those reported for α-$NbPO_5$ (~1.7 V vs. Li^+/Li^0) and β-$NbPO_5$ (~2 V vs. Li^+/Li^0).[51] From this, we deduce Nb redox is not involved in the 3.5 redox reaction. As for the oxidation state of V, there is predominantly V^{4+} in the as-synthesized substituted material (Figure 13d-f). A significant edge shift towards lower energy (5467.5 eV) and a reduction in the pre-edge peak intensity are observed during the discharge to 1.6 V, consistent with the reduction of V^{4+}. In the XANES spectra for octahedrally coordinated V^{3+} compounds where the electric dipole transition to the lowest empty state (1s → 3d) is forbidden by the selection rule, a weaker pre-edge intensity that corresponds to a less symmetric octahedral V coordination is typically observed.[52] Therefore, the experimental results are consistent with the formation of a V^{3+} environment by the end of discharge. As the sample is charged back, the pre-edge peak (5469 eV) intensities increase, with the main edges shifting back to higher energy, representing V oxidation. Upon fully charging to 4.5 V, the pre-edge peak (5470.6 eV) is at the same energy as

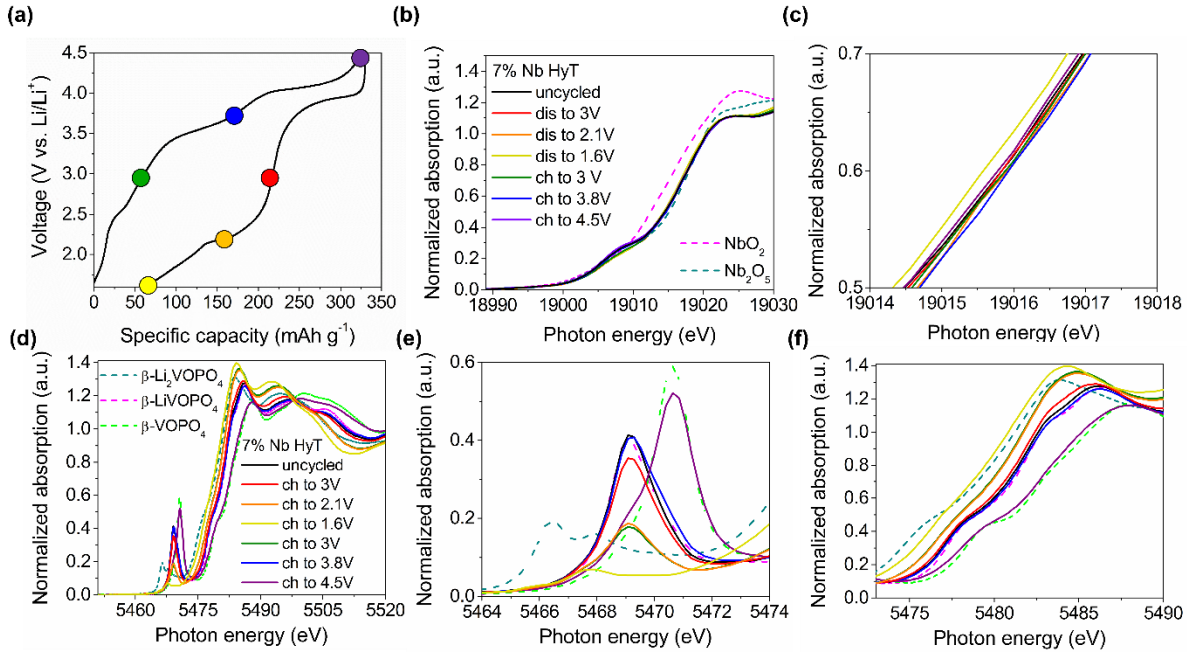

Figure 13. (a) Galvanostatic curve showing the different states of charge and discharge at which cells were recovered for ex-situ XAS measurements. XAS spectra of electrochemically-cycled 7% Nb-substituted HyT $LiVOPO_4$ at the (b-c) Nb and (d-f) V K-edges.

the β-$V^{5+}OPO_4$ standard, with a shoulder at lower energy (5470 eV), suggestive of residual V^{4+} in the sample. These observations align with the galvanostatic charge-discharge tests that indicate less than 2 Li^+ extraction per f.u. of the 7% Nb-substituted sample. On the other hand, the pre-edge peak of the 5% Nb-substituted sample (Figure S17c) overlaps with the β-$VOPO_4$ standard, showing complete oxidation to V^{5+} by the end of charge. A detailed evaluation of the XANES spectra at the V K-edge reveals an appreciable difference in the pre-edge feature between the samples charged and discharged to the same potential of 3 V (Figure S18). The sample charged to 3 V shows a significantly decreased peak intensity compared to the sample discharged to 3 V. The pre-edge intensity of the sample charged to 3 V overlaps well with those discharged to 2.1 V; the stronger intensity of the sample discharged to 3 V matches better with those charged to 3.8 V. This mismatch supports the assignment of the 3.5 V feature, observed in Figure 12, to oxidation of lower valent V-ion to V^{4+}.

Ex-situ PDF measurements were carried out to cross-validate the assignment of the 3.5 V process by probing the local structural changes in the Nb-substituted samples during Li cycling. (Figure 14b) Single peak fitting was performed for the first two peaks (< 2.2 Å) to obtain the average P-O and TM-O bond lengths. When cycled within 1.6 - 4.5 V, the positions of Peak 1 (assigned to the P-O bond) remain at ~1.54 Å, which is consistent with the invariance of the P-O bonds of the phosphate group. For Peak 2 (assigned to the TM-O bond), there is a continuous shift towards lower r from 2.01 Å to 1.92

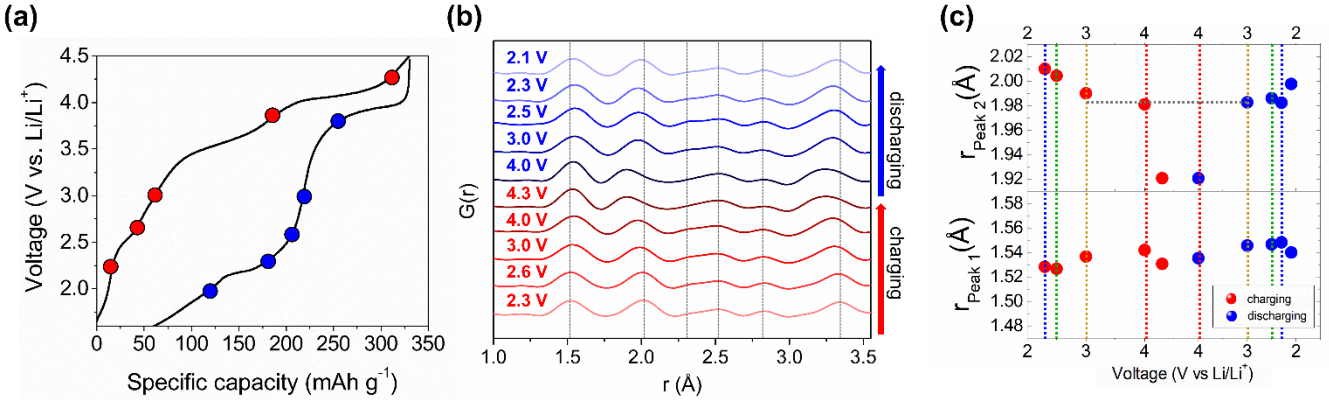

Figure 14. (a) Galvanostatic curve showing the different states of charge and discharge at which cells were recovered for ex-situ PDF measurements. (b) X-ray PDF patterns obtained at different states of charge for 7% Nb-substituted HyT $LiVOPO_4$ and (c) the interatomic distances of the first two peaks as a function of voltage. Dashed vertical lines of matching colors correspond to samples recovered at the same potentials; dashed horizontal line shows the difference between samples charged and discharged to 3 V. Error bars are smaller than the symbols.

Å when charged from 2.3 V to 4.3 V, which corresponds to the shortening of the V-O bond (or decreased ionic radius of V) with increasing V oxidation state. The opposite trend is observed for the V-O bond during discharge, consistent with the reduction of V during discharge. Similar to the XAS results, there are discrepancies in the interatomic distances of Peak 2 between samples recovered at the same voltage (Figure 14c). The most pronounced difference is observed for samples recovered at 4.0 V, where the TM-O bond length is 1.98 Å for the sample recovered upon charge as opposed to 1.92 Å for the sample recovered upon discharge. However, this is attributed to the polarization of the high-voltage plateau as evidenced by a substantially lower capacity obtained during discharge. Another difference is observed for the samples recovered at 3 V, where the TM-O bond length for 3 V on discharge is slightly closer to V^{4+}-O bond length than 3 V on charge (Figure S19), which cross-validates the partial redox between V^{4+} and the lower valent V ions as the origin of the 3.5 V feature.

4. Conclusions

The addition of Nb during the hydrothermal method leads to a new phase, β'-$LiVOPO_4$, with the *Pmn2₁* space group that has not been reported in (Li)$VOPO_4$. Closely related to the β-$LiVOPO_4$ polymorph, this new phase has a lower symmetry that likely arises from either or a combination of ordered V vacancies, incorporation of protons, and some Nb ordering on the V site. The joint XRD and NPD refinement results confirmed the successful substitution of Nb for V at the V site. The defect chemistry of the Nb-substituted samples was investigated by ICP-OES, CHNS, TG-MS, XAS, and SQUID. There was a decrease in the amount of Li and V, along with a simultaneous increase in H^+ content, as more Nb^{5+} was added during synthesis. However, Nb is likely not responsible for the formation of all defects because H^+ is intrinsic to hydrothermally-prepared $LiVOPO_4$. The Nb-substituted samples demonstrate improved specific capacity and capacity retention despite the large voltage hysteresis in the low voltage region. We have found that the low-voltage hysteresis is associated with the redox reaction between V^{4+} and lower valent V ions by a combination of ex-situ XAS and PDF measurements. Our study demonstrates the complexity of defects that can be introduced by a seemingly straightforward elemental substitution synthesis. The complex defect chemistry undermines the effort to deconvolute the contributions of individual defects to elucidate the structure-function relationship. Therefore, future studies on the substitutional effect should eliminate undesired defects in the substituted phase, such as protons and V/Nb_{Li}. Our results suggest that similar studies on $LiVOPO_4$ should be limited to high-temperature synthesized products to easily investigate the effects of the substituent for the purpose of fundamental research.

Conflicts of interest

There are no conflicts to declare.

Supporting Information

Summary of the elemental composition of Nb-substituted HyT $LiVOPO_4$; H/P and C/P molar ratio calculations from TG-MS and CHNS data; FT-IR spectra of Nb-substituted samples; XRD patterns of $LiVOPO_4$ samples before and after the addition of the Nb precursor during hydrothermal synthesis; comparison of lattice parameters of pristine HyTA and Nb-substituted HyT $LiVOPO_4$ with literature; details of combined Rietveld refinement analysis for Nb-substituted HyT $LiVOPO_4$; PDF structural model for β-$LiVOPO_4$; magnetic parameters obtained by the Curie-Weiss Law for Nb-substituted HyT $LiVOPO_4$; Curie constants and effective magnetic moments calculations based on two theoretical models; summary of cationic charges for H analysis; SEM images of pristine HyTA and Nb-substituted HyT $LiVOPO_4$ after high-energy ball-milling; GITT measurements of pristine HyTA and Nb-substituted HyT $LiVOPO_4$; ex-situ XAS and PDF of electrochemically charged and discharged Nb-substituted HyT $LiVOPO_4$; comparison of interatomic distances of Nb-substituted HyT $LiVOPO_4$ during the electrochemical process of 1.6 - 4.5 V with literature.

Author Information

Corresponding Authors

*Email: liuh@binghamton.edu, stanwhit@gmail.com

ORCID

Krystal Lee: 0000-0002-7132-3785

Hui Zhou: 0000-0001-8739-963X

Carol Kaplan: 0000-0001-7164-387X

Natasha A. Chernova: 0000-0002-4855-3224

Hao Liu: 0000-0003-0345-6647

M. Stanley Whittingham: 0000-0002-5039-9334

Acknowledgements

This work was supported as part of NECCES, an Energy Frontier Research Center funded by the U.S. Department of Energy, Office of Science, Office of Basic Energy Sciences under award number DE-SC0012583. This work was also supported by LG Energy Solutions under award number 92617. This research used resources from the Advanced Photon Source, a U.S. Department of Energy (DOE) Office of Science User Facility operated for the DOE Office of Science by Argonne National Laboratory under Contract No. DE-AC02-06CH11357. The mail-in program of Beamline 11-BM and Beamline 11-ID-B contributes to the high-resolution XRD and X-ray PDF data, respectively. A portion of this research used resources at the

Spallation Neutron Source, a DOE Office of Science User Facility operated by the Oak Ridge National Laboratory at Beamline 11A POWGEN for the neutron diffraction data. We thank Dr. Jue Liu for the helpful discussion on neutron refinement. This research also used resources from the Diamond Light Source at Diamond House, Harwell Science and Innovation Campus at Beamline 18. We thank Dr. Giannantonio Cibin for the help with the XAS measurements. We would also like to thank Professor Louis F.J. Piper and his team for help on X-ray-based spectroscopy measurements and analysis during his time at Binghamton University.

References

1. Whittingham, M. S. Lithium Batteries and Cathode Materials. *Chem. Rev.* 2004, **104** (10), 4271–4302. https://doi.org/10.1021/cr020731c.
2. Whittingham, M. S. Ultimate Limits to Intercalation Reactions for Lithium Batteries. *Chem. Rev.* 2014, *114* (23), 11414–11443. https://doi.org/10.1021/cr5003003.
3. Whittingham, M. S.; Siu, C.; Ding, J. Can Multielectron Intercalation Reactions Be the Basis of Next Generation Batteries? *Acc. Chem. Res.* 2018, **51** (2), 258–264. https://doi.org/10.1021/acs.accounts.7b00527.
4. Chernova, N. A.; Hidalgo, M. F. V.; Kaplan, C.; Lee, K.; Buyuker, I.; Siu, C.; Wen, B.; Ding, J.; Zuba, M.; Wiaderek, K. M.; Seymour, I. D.; Britto, S.; Piper, L. F. J.; Ong, S. P.; Chapman, K. W.; Grey, C. P.; Whittingham, M. S. Vanadyl Phosphates A_xVOPO_4 (A = Li, Na, K) as Multielectron Cathodes for Alkali-Ion Batteries. *Adv. Energy Mater.* 2020, **10** (47), 2002638. https://doi.org/10.1002/aenm.202002638.
5. Hautier, G.; Jain, A.; Ong, S. P.; Kang, B.; Moore, C.; Doe, R.; Ceder, G. Phosphates as Lithium-Ion Battery Cathodes: An Evaluation Based on High-Throughput *Ab Initio* Calculations. *Chem. Mater.* 2011, **23** (15), 3495–3508. https://doi.org/10.1021/cm200949v.
6. He, G.; Bridges, C. A.; Manthiram, A. Crystal Chemistry of Electrochemically and Chemically Lithiated Layered α_I-$LiVOPO_4$. *Chem. Mater.* 2015, **27** (19), 6699–6707. https://doi.org/10.1021/acs.chemmater.5b02609.
7. Shahul Hameed, A.; Nagarathinam, M.; Reddy, M. V.; Chowdari, B. V. R.; Vittal, J. J. Synthesis and Electrochemical Studies of Layer-Structured Metastable α_I-$LiVOPO_4$. *J. Mater. Chem.* 2012, **22** (15), 7206. https://doi.org/10.1039/c2jm00062h.
8. Lii, K. H.; Li, C. H.; Cheng, C. Y.; Wang, S. L. Hydrothermal Synthesis, Structure, and Magnetic Properties of a New Polymorph of Lithium Vanadyl (IV) Orthophosphate: β-$LiVOPO_4$. *J Solid State Chem* 1991, **95**, 352–359. https://doi.org/10.1016/0022-4596(91)90116-Y.
9. Barker, J.; Saidi, M. Y.; Swoyer, J. L. Electrochemical Properties of Beta-$LiVOPO_4$ Prepared by Carbothermal Reduction. *Journal of The Electrochemical Society* 2004, **151** (6), A796–A800. https://doi.org/10.1149/1.1723494.
10. (Azmi, B. M.; Ishihara, T.; Nishiguchi, H.; Takita, Y. $LiVOPO_4$ as a New Cathode Materials for Li-Ion Rechargeable Battery. *Journal of Power Sources* 2005, **146**, 525–528. https://doi.org/10.1016/j.jpowsour.2005.03.101.
11. Britto, S.; Seymour, I. D.; Halat, D. M.; Hidalgo, M. F. V.; Siu, C.; Reeves, P. J.; Zhou, H.; Chernova, N. A.; Whittingham, M. S.; Grey, C. P. Evolution of Lithium Ordering with (de)-Lithiation in β-$LiVOPO_4$: Insights through Solid-State NMR and First Principles DFT Calculations. *J. Mater. Chem. A* 2020, **8** (11), 5546–5557. https://doi.org/10.1039/D0TA00121J.
12. Chung, Y.; Cassidy, E.; Lee, K.; Siu, C.; Huang, Y.; Omenya, F.; Rana, J.; Wiaderek, K. M.; Chernova, N. A.; Chapman, K. W.; Piper, L. F. J.; Whittingham, M. S. Nonstoichiometry and Defects in Hydrothermally Synthesized ε-$LiVOPO_4$. *ACS Appl. Energy Mater.* 2019, **2** (7), 4792–4800. https://doi.org/10.1021/acsaem.9b00448.
13. Rana, J.; Shi, Y.; Zuba, M. J.; Wiaderek, K. M.; Feng, J.; Zhou, H.; Ding, J.; Wu, T.; Cibin, G.; Balasubramanian, M.; Omenya, F.; Chernova, N. A.; Chapman, K. W.; Whittingham, M. S.; Piper, L. F. J. Role of Disorder in Limiting the True Multi-Electron Redox in ε-$LiVOPO_4$. *J. Mater. Chem. A* 2018, **6** (42), 20669–20677. https://doi.org/10.1039/C8TA06469E.
14. Zhou, H.; Shi, Y.; Xin, F.; Omenya, F.; Whittingham, M. S. ε- and β-$LiVOPO_4$: Phase Transformation and Electrochemistry. *ACS Appl. Mater. Interfaces* 2017, **9** (34), 28537–28541. https://doi.org/10.1021/acsami.7b07895.
15. Nojima, A.; Sano, A.; Fujita, S.; Ohtsuki, K.; Okada, S. Evaluation of α_1-$LiVOPO_4$, β-$LiVOPO_4$, and α-$LiVOPO_4$ Synthesized from a Same Precursor by Hydrothermal Method. *J. Electrochem. Soc.* 2019, **166** (15), A3731–A3738. https://doi.org/10.1149/2.0691915jes.
16. Shi, Y.; Zhou, H.; Seymour, I. D.; Britto, S.; Rana, J.; Huang, Y.; Yin, Q.; Reeves, P. J.; Zuba, M.; Chung, Y.; Omenya, F.; Chernova, N. A.; Zhou, G.; Piper, L. F. J.; Grey, C. P.; Whittingham, M. S. Electrochemical Performance of Nanosized Disordered $LiVOPO_4$. *ACS Omega* 2018, **3**, 7310–7323.
17. Shi, Y.; Zhou, H.; Britto, S.; Seymour, I. D.; Wiaderek, K. M.; Omenya, F.; Chernova, N. A.; Chapman, K. W.; Grey, C. P.; Whittingham, M. S. A High-Performance Solid-State Synthesized $LiVOPO_4$ for Lithium-Ion Batteries. *Electrochemistry Communications* 2019, **105**, 106491. https://doi.org/10.1016/j.elecom.2019.106491.
18. Hidalgo, M. F. V.; Lin, Y.-C.; Grenier, A.; Xiao, D.; Rana, J.; Tran, R.; Xin, H.; Zuba, M.; Donohue, J.; Omenya, F. O.; Chu, I.-H.; Wang, Z.; Li, X.; Chernova, N. A.; Chapman, K. W.; Zhou, G.; Piper, L.; Ong, S. P.; Whittingham, M. S. Rational Synthesis and Electrochemical Performance of $LiVOPO_4$ Polymorphs. *J. Mater. Chem. A* 2019, **7** (14), 8423–8432. https://doi.org/10.1039/C8TA12531G.
19. Lin, Y.-C.; Wen, B.; Wiaderek, K. M.; Sallis, S.; Liu, H.; Lapidus, S. H.; Borkiewicz, O. J.; Quackenbush, N. F.; Chernova, N. A.; Karki, K.; Omenya, F.; Chupas, P. J.; Piper, L. F. J.; Whittingham, M. S.; Chapman, K. W.; Ong, S. P. Thermodynamics, Kinetics and Structural Evolution of ε-$LiVOPO_4$ over Multiple Lithium Intercalation. *Chem. Mater.* 2016, **28** (6), 1794–1805. https://doi.org/10.1021/acs.chemmater.5b04880.
20. Ren, M. M.; Zhou, Z.; Su, L. W.; Gao, X. P. $LiVOPO_4$: A Cathode Material for 4V Lithium Ion Batteries. *Journal of Power Sources* 2009, **189** (1), 786–789. https://doi.org/10.1016/j.jpowsour.2008.07.092.
21. Harrison, K. L.; Bridges, C. A.; Segre, C. U.; Varnado, C. D.; Applestone, D.; Bielawski, C. W.; Paranthaman, M. P.; Manthiram, A. Chemical and Electrochemical Lithiation of $LiVOPO_4$ Cathodes for Lithium-Ion Batteries. *Chem. Mater.* 2014, **26** (12), 3849–3861. https://doi.org/10.1021/cm501588j.
22. Kaplan, C.; Hidalgo, M. F. V.; Zuba, M. J.; Chernova, N. A.; Piper, L. F. J.; Whittingham, M. S. Microwave-Assisted Solvothermal Synthesis of $LiV_yM_{1-y}OPO_4$ (M = Mn, Cr, Ti, Zr, Nb, Mo, W) Cathode Materials for Lithium-Ion Batteries. *J. Mater. Chem. A* 2021, **9** (11), 6933–6944. https://doi.org/10.1039/D0TA11704H.

23. Bianchini, M.; Ateba-Mba, J. M.; Dagault, P.; Bogdan, E.; Carlier, D.; Suard, E.; Masquelier, C.; Croguennec, L. Multiple Phases in the ε-VPO_4O–$LiVPO_4O$–Li_2VPO_4O System: A Combined Solid State Electrochemistry and Diffraction Structural Study. *J. Mater. Chem. A* 2014, **2** (26), 10182–10192. https://doi.org/10.1039/C4TA01518E.
24. Siu, C.; Seymour, I. D.; Britto, S.; Zhang, H.; Rana, J.; Feng, J.; Omenya, F. O.; Zhou, H.; Chernova, N. A.; Zhou, G.; Grey, C. P.; Piper, L. F. J.; Whittingham, M. S. Enabling Multi-Electron Reaction of ε-$VOPO_4$ to Reach Theoretical Capacity for Lithium-Ion Batteries. *Chem. Commun.* 2018, **54** (56), 7802–7805. https://doi.org/10.1039/c8cc02386g.
25. Dunne, P. W.; Munn, A. S.; Starkey, C. L.; Huddle, T. A.; Lester, E. H. Continuous-Flow Hydrothermal Synthesis for the Production of Inorganic Nanomaterials. *Phil. Trans. R. Soc. A.* 2015, **373** (2057), 20150015. https://doi.org/10.1098/rsta.2015.0015.
26. Cundy, C. S.; Cox, P. A. The Hydrothermal Synthesis of Zeolites: History and Development from the Earliest Days to the Present Time. *Chem. Rev.* 2003, **103** (3), 663–702. https://doi.org/10.1021/cr020060i.
27. Lee, K.; Siu, C.; Hidalgo, M. F. V.; Rana, J.; Zuba, M.; Chung, Y.; Omenya, F.; Piper, L. F. J.; Liu, H.; Chernova, N. A.; Whittingham, M. S. Structure, Composition, and Electrochemistry of Chromium-Substituted ε-$LiVOPO_4$. *ACS Appl. Energy Mater.* 2021, **4** (2), 1421–1430. https://doi.org/10.1021/acsaem.0c02634.
28. Wen, B.; Wang, Q.; Lin, Y.; Chernova, N. A.; Karki, K.; Chung, Y.; Omenya, F.; Sallis, S.; Piper, L. F. J.; Ong, S. P.; Whittingham, M. S. Molybdenum Substituted Vanadyl Phosphate ε-$VOPO_4$ with Enhanced Two-Electron Transfer Reversibility and Kinetics for Lithium-Ion Batteries. *Chem. Mater.* 2016, **28** (9), 3159–3170. https://doi.org/10.1021/acs.chemmater.6b00891.
29. Siu, C.; Zuba, M. J.; Zong, Y.; Zhou, H.; Chernova, N. A.; Piper, L. F. J.; Zhou, G.; Whittingham, M. S. Enhanced High-Rate Performance of Nanosized Single Crystal ε-$VOPO_4$ with Niobium Substitution for Lithium-Ion Batteries. *J. Electrochem. Soc.* 2021, **168** (6), 060519. https://doi.org/10.1149/1945-7111/ac035f.
30. Lee, S.-H.; Ryu, K.-S. Effects of Ti Doping on the Structural Stability and Enhanced Electrochemical Performance of α-$LiVOPO_4$. *Bull. Korean Chem. Soc.* 2018, **39** (11), 1266–1272. https://doi.org/10.1002/bkcs.11586.
31. Xiong, L.; Wang, Y.; Wu, Y.; Liu, W.; He, Z. Enhanced Electrochemical Performance of Manganese-Doped β-$LiVOPO_4$ Cathode Materials for Lithium-Ion Batteries. *Ionics* 2015, **21** (9), 2471–2476. https://doi.org/10.1007/s11581-015-1436-9.
32. Park, D.-J.; Rajagopal, R.; Ryu, K.-S. Effects of Zr Doping to Improve Ionic Conductivity and Lithium-Diffusion Kinetics of β-$LiVOPO_4$ Cathode Material. *Journal of Industrial and Engineering Chemistry* 2020, **83**, 260–270. https://doi.org/10.1016/j.jiec.2019.11.036.
33. Bustam, M. A.; Man, Z.; Maitra, S.; Ishihara, T. Electrochemical Performance of Cathode $LiVOPO_4$ Doped with Mo and W. *Transactions of the Indian Ceramic Society* 2013, **72** (2), 108–112. https://doi.org/10.1080/0371750X.2013.794029.
34. Dean, J. A. *Lange's Handbook of Chemistry*, 16th ed.; McGraw-Hill Professional, 1979.
35. Coelho, A. A. TOPAS and TOPAS-Academic: An Optimization Program Integrating Computer Algebra and Crystallographic Objects Written in C++. 2018, **51**, 210–218. https://doi.org/doi.org/10.1107/S1600576718000183.
36. Juhás, P.; Davis, T.; Farrow, C. L.; Billinge, S. J. L. *PDFgetX3* : A Rapid and Highly Automatable Program for Processing Powder Diffraction Data into Total Scattering Pair Distribution Functions. *J Appl Crystallogr* 2013, **46** (2), 560–566. https://doi.org/10.1107/S0021889813005190.
37. Stokes, H. T.; Hatch, D. M.; Campbell, B. J. ISOTROPY Software Suite. iso.byu.edu.
38. Phadke, S.; Nino, J. C.; Islam, M. S. Structural and Defect Properties of the $LaPO_4$ and LaP_5O_{14}-Based Proton Conductors. *J. Mater. Chem.* 2012, **22** (48), 25388. https://doi.org/10.1039/c2jm32940a.
39. Granada, J. R. Neutron Thermalization in H_2O and D_2O with the Use of a Synthetic Scattering Function. *Phys. Rev. B* 1985, **32** (11), 7555–7557. https://doi.org/10.1103/PhysRevB.32.7555.
40. Boivin, E.; Chotard, J.-N.; Ménétrier, M.; Bourgeois, L.; Bamine, T.; Carlier, D.; Fauth, F.; Suard, E.; Masquelier, C.; Croguennec, L. Structural and Electrochemical Studies of a New Tavorite Composition: $LiVPO_4OH$. *J. Mater. Chem. A* 2016, **4** (28), 11030–11045. https://doi.org/10.1039/C6TA03339C.
41. Marx, N.; Croguennec, L.; Carlier, D.; Bourgeois, L.; Kubiak, P.; Cras, F. L.; Delmas, C. Structural and Electrochemical Study of a New Crystalline Hydrated Iron(III) Phosphate $FePO_4{\cdot}H_2O$ Obtained from $LiFePO_4(OH)$ by Ion Exchange. *Chem. Mater.* 2010, **22** (5), 1854–1861. https://doi.org/10.1021/cm903370z.
42. Kang, B.; Zhu, Q. Spin–Spin Interaction in ε-$VOPO_4$ through Doping Light Elements. *J. Phys. Chem. C* 2022, **126** (49), 21034–21039. https://doi.org/10.1021/acs.jpcc.2c05979.
43. Lim, S. C.; Vaughey, J. T.; Harrison, W. T. A.; Dussack, L. L.; Jacobson, A. J.; Johnson, J. W. Redox Transformations of Simple Vanadium Phosphates: The Synthesis of ε-$VOPO_4$. *Solid State Ion* 1996, **84**, 219–226. https://doi.org/10.1016/0167-2738(96)00007-0.
44. Vaughey, J. T.; Harrison, W. T. A.; Jacobson, A. J.; Goshorn, D. P.; Johnson, J. W. Synthesis, Structure, and Properties of Two New Vanadium (III) Phosphates: $VPO_4{\cdot}H_2O$ and $V_{1.23}(PO_4)(OH)_{0.69}(H_2O)_{0.31}{\cdot}0.33H_2O$. *Inorg. Chem.* 1994, **33** (11), 2481–2487. https://doi.org/10.1021/ic00089a027.
45. Shahul Hameed, A.; Nagarathinam, M.; Reddy, M. V.; Chowdari, B. V. R.; Vittal, J. J. Synthesis and Electrochemical Studies of Layer-Structured Metastable α_I-$LiVOPO_4$. *J. Mater. Chem.* 2012, **22** (15), 7206. https://doi.org/10.1039/c2jm00062h.
46. Liao, J.; Hu, Q.; Che, B.; Ding, X.; Chen, F.; Chen, C. Competing with Other Polyanionic Cathode Materials for Potassium-Ion Batteries *via* Fine Structure Design: New Layered $KVOPO_4$ with a Tailored Particle Morphology. *J. Mater. Chem. A* 2019, **7** (25), 15244–15251. https://doi.org/10.1039/C9TA03192H.
47. Amos, T. G.; Yokochi, A. F. T.; Sleight, A. W. Phase Transition and Negative Thermal Expansion in Tetragonal $NbOPO_4$. *J. Solid State Chem.* 1998, **141**, 303–307.
48. Yang, Y.; Fang, H.; Zheng, J.; Li, L.; Li, G.; Yan, G. Towards the Understanding of Poor Electrochemical Activity of Triclinic $LiVOPO_4$: Experimental Characterization and Theoretical Investigations. *Solid State Sciences* 2008, **10** (10), 1292–1298. https://doi.org/10.1016/j.solidstatesciences.2008.01.028.
49. Ford, P. J. Spin Glasses. *Contemporary Physics* 1982, **23** (2), 141–168. https://doi.org/10.1080/00107518208237073.
50. Lin, Y.-C.; Hidalgo, M. F. V.; Chu, I.-H.; Chernova, N. A.; Whittingham, M. S.; Ong, S. P. Comparison of the Polymorphs of $VOPO_4$ as Multi-Electron Cathodes for Rechargeable Alkali-Ion Batteries. *J. Mater. Chem. A* 2017, **5** (33), 17421–17431. https://doi.org/10.1039/C7TA04558A.
51. Patoux, S.; Masquelier, C. Chemical and Electrochemical Insertion of Lithium into Two Allotropic Varieties of $NbPO_5$.

Chem. Mater. 2002, **14** (5), 2334–2341. https://doi.org/10.1021/cm010398d.

52. Duchesne, M. A.; Nakano, J.; Hu, Y.; MacLennan, A.; Bennett, J.; Nakano, A.; Hughes, R. W. Synchrotron-Based X-Ray Absorption Spectroscopy Study of Vanadium Redox Speciation during Petroleum Coke Combustion and Gasification. *Fuel* 2018, **227**, 279–288. https://doi.org/10.1016/j.fuel.2018.04.104.